Stars and their variability observed from space
C. Neiner, W. Weiss, D. Baade, E. Griffin, C. Lovekin, A. Moffat (eds)

NEW FULLY EVOLUTIONARY MODELS FOR ASTEROSEISMOLOGY OF ULTRA-MASSIVE WHITE DWARF STARS

A. H. Córsico[1,2], F. C. De Gerónimo[1,2], M. E. Camisassa[1,2] and L. G. Althaus[1,2]

Abstract. Ultra-massive hydrogen-rich (DA spectral type) white dwarf (WD) stars ($M_\star > 1 M_\odot$) coming from single-star evolution are expected to harbor cores made of ^{16}O and ^{20}Ne, resulting from semi-degenerate carbon burning when the progenitor star evolves through the super asymptotic giant branch (S-AGB) phase. These stars are expected to be crystallized by the time they reach the ZZ Ceti instability strip ($T_{\rm eff} \sim 12\,500$ K). Theoretical models predict that crystallization leads to a separation of ^{16}O and ^{20}Ne in the core of ultra-massive WDs, which impacts their pulsational properties. This property offers a unique opportunity to study the processes of crystallization. Here, we present the first results of a detailed asteroseismic analysis of the best-studied ultra-massive ZZ Ceti star BPM 37093. As a second step, we plan to repeat this analysis using ultra-massive DA WD models with C/O cores in order to study the possibility of elucidating the core chemical composition of BPM 37093 and shed some light on its possible evolutionary origin. We also plan to extend this kind of analyses to other stars observed from the ground and also from space missions like Kepler and TESS.

Keywords: stars: pulsations, stars: interiors, stars: white dwarfs

1 Input physics, evolution/pulsation codes, and stellar models

The evolutionary models were generated by Camisassa et al. (2019) employing the `LPCODE` evolutionary code. The evolutionary tracks are shown in Fig. 1. The input physics of `LPCODE` is described in Camisassa et al. (2019) and we refer the interested reader to that paper for details. Of particular importance in this work is the treatment of crystallization. Cool WD stars are supposed to crystallize due to the strong Coulomb interactions in their very dense interior (van Horn 1968). In our models, crystallization sets in when the energy of the Coulomb interaction between neighboring ions is much higher than their thermal energy. The release of latent heat, and the release of gravitational energy associated with changes in the chemical composition profile induced by crystallization, are consistently taken into account. The chemical redistribution due to phase separation and the associated release of energy have been considered following Althaus et al. (2010), appropriately modified by (van Horn 1968) for ONe plasmas. To assess the enhancement of ^{20}Ne in the crystallized core, we used the azeotropic-type phase diagram of Medin & Cumming (2010). The pulsation code used to compute nonradial g(gravity)-mode pulsations is the adiabatic version of the `LP-PUL` pulsation code described in Córsico & Althaus (2006). To account for the effects of crystallization on the pulsation spectrum of g modes, we adopted the "hard sphere" boundary conditions (see Montgomery & Winget 1999). Our ultra-massive WD models have stellar masses $M_\star = 1.10, 1.16, 1.22$, and $1.29 M_\odot$. They result from the complete evolution of the progenitor stars through the S-AGB phase. The core and inter- shell chemical profiles of our models at the start of the WD cooling phase were obtained from Siess (2010).

2 Chemical profiles and the Brunt-Väisälä frequency

The cores of our models are composed mostly of ^{16}O and ^{20}Ne and smaller amounts of ^{12}C, ^{23}Na, and ^{24}Mg. Since element diffusion and gravitational settling operate throughout the WD evolution, our models develop

[1] Facultad de Ciencias Astronómicas y Geofísicas, Universidad Nacional de La Plata, Paseo delBosque s/n, (1900), La Plata, Argentina
[2] Instituto de Astrofísica de La Plata, IALP, CONICET-UNLP, La Plata, Argentina

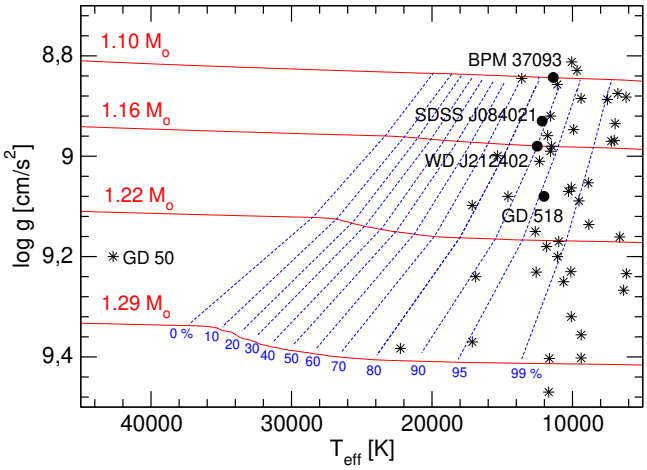

Fig. 1. Evolutionary tracks (red solid lines) of the ultra-massive DA WD models computed by Camisassa et al. (2019) in the $T_{\rm eff} - \log g$ plane. Blue dashed lines indicate 0, 10, 20, 30, 40, 50, 60, 70, 80, 90, 95 and 99 % of crystallized mass. The location of ultra-massive DA WD stars are indicated with black star symbols, and the ultra-massive ZZ Ceti stars are emphasized with black circles.

pure H envelopes. The He content of our WD sequences is given by the evolutionary history of progenitor star, but instead, the H content of our canonical envelopes [$\log(M_{\rm H}/M_\star = -6$] has been set by imposing that the further evolution does not lead to H thermonuclear flashes on the WD cooling track. We have expanded our grid of models by artificially generating new sequences with thinner H envelopes [$\log(M_{\rm H}/M_\star = -7, -8, -9, -10$], for each stellar mass value. This artificial procedure has been done at high-luminosity stages of the WD evolution. The temporal changes of the chemical abundances due to element diffusion are assessed by using a new full-implicit treatment for time-dependent element diffusion (Althaus et al. 2020).

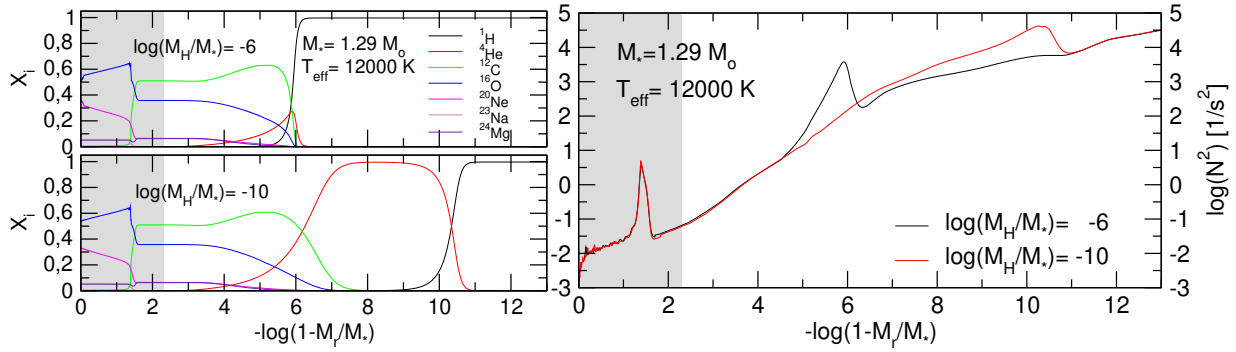

Fig. 2. Left: Abundances by mass of the different chemical species as a function of the fractional mass, corresponding to ONe-core WD models with $M_\star = 1.29 M_\odot$, $T_{\rm eff} \sim 12\,000$ K and two different H envelope thicknesses, as indicated. The percentage of crystallized mass fraction of the models is 99.5 % (gray region). **Right:** Logarithm of the squared Brunt-Väisälä frequency, corresponding to the same ONe-core WD models with $M_\star = 1.29 M_\odot$, $T_{\rm eff} \sim 12\,000$ K and $\log(M_{\rm H}/M_\star) = -6$, and -10 shown in the left panel.

The chemical profiles in terms of the fractional mass for $1.29 M_\star$ ONe-core WD models at $T_{\rm eff} \sim 12\,000$ K and H envelope thicknesses $\log(M_{\rm H}/M_\star) = -6$ and -10 are shown in the left panel of Fig. 2. A pure He buffer develops as we consider thinner H envelopes. At this effective temperature, the chemical rehomogeneization due to crystallization has already finished, giving rise to a core where the abundance of ^{16}O (^{20}Ne) increases (decreases) outward. In the right panel of Fig. 2 we show the logarithm of the squared Brunt-Väisälä frequency corresponding to the same models shown in the left panel of the figure. The peak at $-\log(1 - M_r/M_\star) \sim 1.4$, which is due to the abrupt step at the triple chemical transition between ^{12}C, ^{16}O, and ^{20}Ne, is within the solid part of the core, so it has no relevance for the mode-trapping properties of the models. This is because, according to the hard-sphere boundary conditions adopted for the pulsations, the eigenfunctions of g modes

Table 1. Frequencies and periods of BPM 37093 (Metcalfe et al. 2004), along with the theoretical periods, harmonic degrees, radial orders, and period differences of our best-fit model.

$\Pi^{\rm O}$ [sec]	ν [μHz]	$\Pi^{\rm T}$ [sec]	ℓ	k	δ_i [sec]
511.7	1954.1	512.4	2	29	−0.7
531.1	1882.9	531.9	1	17	−0.8
548.4	1823.5	548.1	2	31	0.3
564.1	1772.7	565.3	2	32	−1.2
582.0	1718.2	583.0	2	33	−1.0
600.7	1664.9	599.9	2	34	0.8
613.5	1629.9	613.8	1	20	−0.3
635.1	1574.6	632.2	2	36	2.9

Table 2. The main characteristics of BPM 37093

Quantity	Spectroscopy	Asteroseismology
$T_{\rm eff}$ [K]	$11\,370 \pm 500$	$11\,650 \pm 40$
$M_\star/M_\odot$	1.098 ± 0.1	1.16 ± 0.014
$\log g$ [cm/s^2]	8.843 ± 0.05	8.970 ± 0.025
$\log(L_\star/L_\odot)$	—	-3.25 ± 0.01
$\log(R_\star/R_\odot)$	—	-2.234 ± 0.006
$\log(M_{\rm H}/M_\star)$	—	-6 ± 0.26
$\log(M_{\rm He}/M_\star)$	—	-3.8
$M_{\rm cr}/M_\star$	0.935	0.923
$X_{^{16}{\rm O}}$ cent.	—	0.52
$X_{^{20}{\rm Ne}}$ cent.	—	0.34
Quantity	Measured	Asteroseismology
$\overline{\Delta\Pi}_{\ell=1}$ [s]	—	29.70
$\overline{\Delta\Pi}_{\ell=2}$ [s]	17.3 ± 0.9	17.63
Quantity	Astrometry (*Gaia*)	Asteroseismology
d [pc]	14.81	11.32
π [mas]	67.5	88.3

do not penetrate the crystallized region. In this way, the mode trapping properties are entirely determined by the presence of the He/H transition, which is located in more external regions for thinner H envelopes. The pulsation properties of these models have been explored by De Gerónimo et al. (2019) and Córsico et al. (2019).

3 Application: asteroseismological analysis of the ultra-massive ZZ Ceti star BPM 37093

BPM 37093 is the first ultra-massive ZZ Ceti star discovered by Kanaan et al. (1992). This star is characterized by $T_{\rm eff} = 11\,370$ K and $\log g = 8.843$ (Nitta et al. 2016). We searched for a pulsation model that best matches the individual pulsation periods of BPM 37093. The goodness of the match between the theoretical pulsation periods ($\Pi_k^{\rm T}$) and the observed periods ($\Pi_i^{\rm O}$) is measured by means of a merit function defined as $\chi^2(M_\star, M_{\rm H}, T_{\rm eff}) = \frac{1}{N}\sum_{i=1}^{N} \min[(\Pi_i^{\rm O} - \Pi_k^{\rm T})^2]$, where N is the number of observed periods. The WD model that shows the lowest value of χ^2, if exists, is adopted as the "best-fit model". We assumed two possibilities for the mode identification: (i) that all of the observed periods correspond to g modes with $\ell = 1$, and (ii) that the observed periods correspond to a mix of g modes with $\ell = 1$ and $\ell = 2$. We considered the eight periods employed by Metcalfe et al. (2004) (see Table 1). The case (i) did not show clear solutions compatible with BPM 37093 in relation to its spectroscopically-derived effective temperature. Instead, the case (ii) resulted in a clear seismological solution for a WD model with $M_\star = 1.16 M_\odot$, $T_{\rm eff} = 11\,650$ K and $\log(M_{\rm H}/M_\star) = -6$. In Table 1 we show the periods of the best-fit model along with the harmonic degree, the radial order, and the period differences (theoretical minus observed). Most of the periods of BPM 37093 are identified as $\ell = 2$ modes. This is not expected due to geometric cancellation effects (that is, $\ell = 1$ modes should be more easily

detectable than $\ell = 2$ modes). In Table 2, we list the main characteristics of the best-fit model for BPM 37093. The parameters of the best fit model are in agreement with the spectroscopically derived ones. Also, the asteroseismological distance is in line with the astrometric distance obtained from *Gaia*.

A.H.C. warmly thanks the Local Organising Committee, in particular Prof. Werner W. Weiss, for support that allowed him to attend this conference.

References

Althaus, L. G., Córsico, A. H., Uzundag, M., et al. 2020, A&A, 633, A20
Althaus, L. G., García-Berro, E., Renedo, I., et al. 2010, ApJ, 719, 612
Camisassa, M. E., Althaus, L. G., Córsico, A. H., et al. 2019, A&A, 625, A87
Córsico, A. H. & Althaus, L. G. 2006, A&A, 454, 863
Córsico, A. H., De Gerónimo, F. C., Camisassa, M. E., & Althaus, L. G. 2019, A&A, 632, A119
De Gerónimo, F. C., Córsico, A. H., Althaus, L. G., Wachlin, F. C., & Camisassa, M. E. 2019, A&A, 621, A100
Kanaan, A., Kepler, S. O., Giovannini, O., & Diaz, M. 1992, ApJ, 390, L89
Medin, Z. & Cumming, A. 2010, Phys. Rev. E, 81, 036107
Metcalfe, T. S., Montgomery, M. H., & Kanaan, A. 2004, ApJ, 605, L133
Montgomery, M. H. & Winget, D. E. 1999, ApJ, 526, 976
Nitta, A., Kepler, S. O., Chené, A.-N., et al. 2016, IAU Focus Meeting, 29B, 493
Siess, L. 2010, A&A, 512, A10
van Horn, H. M. 1968, ApJ, 151, 227